PCCP

PAPER

Nitrogen defects in wide band gap oxides: defect equilibria and electronic structure from first principles calculations

Jonathan M. Polfus, Tor S. Bjørheim, Truls Norby and Reidar Haugsrud*

The nitrogen related defect chemistry and electronic structure of wide band gap oxides are investigated by density functional theory defect calculations of N_O', $NH_O^\times$, and $(NH_2)_O^\bullet$ as well as $V_O^{\bullet\bullet}$ and $OH_O^\bullet$ in MgO, CaO, SrO, Al_2O_3, In_2O_3, Sc_2O_3, Y_2O_3, La_2O_3, TiO_2, SnO_2, ZrO_2, $BaZrO_3$, and $SrZrO_3$. The N_O' acceptor level is found to be deep and the binding energy of $NH_O^\times$ with respect to N_O' and $OH_O^\bullet$ is found to be significantly negative, *i.e.* binding, in all of the investigated oxides. The defect structure of the oxides was found to be remarkably similar under reducing and nitriding conditions (1 bar N_2, 1 bar H_2 and 1×10^{-7} bar H_2O): $NH_O^\times$ predominates at low temperatures and $[N_O'] = 2[V_O^{\bullet\bullet}]$ predominates at higher temperatures (> 900 K for most of the oxides). Furthermore, we evaluate how the defect structure is affected by non-equilibrium conditions such as doping and quenching. In terms of electronic structure, N_O' is found to introduce isolated N-2p states within the band gap, while the N-2p states of $NH_O^\times$ are shifted towards, or overlap with the VBM. Finally, we assess the effect of nitrogen incorporation on the proton conducting properties of oxides and comment on their corrosion resistance in nitriding atmospheres in light of the calculated defect structures.

1 Introduction

Functional properties of oxide materials are to a large extent coupled to the defect structure of the material and can therefore be tailored through addition of aliovalent dopant ions. The prevalent doping strategy for oxides is introduction of aliovalent cations, which in most cases proves to be simple and effective in promoting the formation of oppositely charged defects. On the other hand, anion dopants, such as nitrogen, can be expected to particularly affect the electronic structure of the valence states and exhibit different characteristics with respect to interaction between the dopant ion and defects associated with anion sites, *e.g.* oxygen vacancies and protons. Furthermore, whereas cation dopants usually are introduced upon synthesis of the materials, nitrogen as an anion dopant may be introduced through equilibration with surrounding gas species such as NH_3. Still, few oxide materials have been characterized in detail with respect to their nitrogen related defect chemistry and corresponding effects on, for instance, electrical and optical properties. Nitrogen is generally expected to dissolve substitutionally in the oxygen lattice and act as an acceptor dopant. The fully ionized nitride ions, N_O' in Kröger–Vink notation, must in turn be charge compensated by effectively positive defects such as electron holes, $h^\bullet$, oxygen vacancies, $V_O^{\bullet\bullet}$, protons, $H_i^\bullet/OH_O^\bullet$, or amide defects, $(NH_2)_O^\bullet$. Nitrogen doping can as such in principle be an effective strategy for p-type doping of oxides. However, there seems to be no unambiguous report where nitrogen is substituted in an oxide and predominately charge compensated by holes despite considerable efforts invested in achieving this within the ZnO system,[1–3] indicating that N_O' to a large extent is charge compensated by various ionic donor defects.

Incorporation of nitrogen in CeO_2,[4] ZrO_2[5] and selected rare-earth tungstates and tantalates[6] has been reported to be accompanied by the formation of oxygen vacancies. In ZrO_2 and the rare-earth based systems this results in the formation of a series of oxide nitride phases due to ordering of the anion lattice.[7–9] However, pre-existing Y-acceptors in yttrium stabilized ZrO_2 prevent this ordering,[10] and the effects of N_O' and Y_{Zr}' are similar except for a stronger acceptor–vacancy interaction in the case of N-doping.[11–13]

Simultaneous incorporation of nitride ions and protons has been demonstrated in ZnO,[14,15] TiO_2,[16] ZrO_2[17] and RE_2O_3 (RE = Nd, Gd, Er and Y).[17] In all cases, the associated defect, $NH_O^\times$ (imide), was favoured over N_O' and $OH_O^\bullet$. The association reaction

$$N_O' + OH_O^\bullet = NH_O^\times + O_O^\times \qquad (1)$$
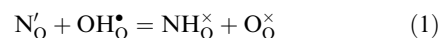
is, accordingly, exothermic. As such, N_O' can act as a proton trap and inhibit proton transport if the dissociation enthalpy

Department of Chemistry, University of Oslo, Centre for Materials Science and Nanotechnology (SMN), FERMiO, Gaustadalléen 21, NO-0349 Oslo, Norway. E-mail: reidarha@kjemi.uio.no
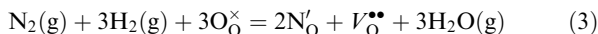
11808 | *Phys. Chem. Chem. Phys.*, 2012, **14**, 11808–11815

This journal is © the Owner Societies 2012

of $NH_O^\times$ is significant. Association with an additional proton is also possible according to

$$NH_O^\times + OH_O^\bullet = (NH_2)_O^\bullet + O_O^\times \tag{2}$$
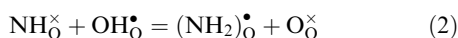
In this respect, we recently reported that $(NH_2)_O^\bullet$ predominates in the unique structure of mayenite, $Ca_{12}Al_{14}O_{33}$, under nitriding conditions[18] in accordance with previous indications.[19] At low temperatures, $(NH_2)_O^\bullet$ was found to be charge compensated by $(NH_2)_i'$ (in the interstitial cages) while they were compensated by N_O' at high temperatures.

In the present work, we utilize density functional theory calculations to investigate the role of various nitrogen defects in a range of binary and ternary oxides. In this respect, we calculate the formation energy of $N_O^\times$, N_O', $NH_O^\times$, and $(NH_2)_O^\bullet$ as well as $V_O^{\bullet\bullet}$ and $OH_O^\bullet$ in rocksalt MgO, CaO and SrO; corundum Al_2O_3; C-type In_2O_3, Sc_2O_3, Y_2O_3 and La_2O_3; rutile TiO_2 and SnO_2; monoclinic ZrO_2; and perovskite $BaZrO_3$ and $SrZrO_3$. The acceptor level for N_O^q (where q is the charge state) and binding energies of $NH_O^\times$ and $(NH_2)_O^\bullet$, *i.e.* enthalpies of reactions (1) and (2), are also considered for all materials. Nitrogen interstitials, N_i''', are considered for a few materials in which oxygen interstitials, O_i'', are important. However, as N_i''' were found to exist in negligible concentrations even in donor doped systems, they were not considered further for all materials.

Further, we evaluate the thermodynamics of nitrogen incorporation according to defect reactions involving three different nitrogen species

$$N_2(g) + 3H_2(g) + 3O_O^\times = 2N_O' + V_O^{\bullet\bullet} + 3H_2O(g) \tag{3}$$

$$N_2(g) + 3H_2(g) + 2O_O^\times = 2NH_O^\times + 2H_2O(g) \tag{4}$$

$$N_2(g) + 3H_2(g) + 2O_O^\times = (NH_2)_O^\bullet + N_O' + 2H_2O(g) \tag{5}$$

In acceptor doped systems where oxygen vacancies predominate, nitrogen can also be incorporated according to

$$N_2(g) + 3H_2(g) + O_O^\times + V_O^{\bullet\bullet} = 2(NH_2)_O^\bullet + H_2O(g) \tag{6}$$
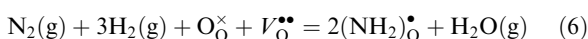
reaction (6) resembles the hydration reaction

$$H_2O(g) + O_O^\times + V_O^{\bullet\bullet} = 2OH_O^\bullet \tag{7}$$
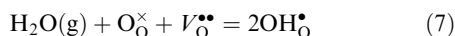
which is important in most of these oxides.

Finally, we assess the changes in the electronic structure of these oxides upon nitrogen and hydrogen incorporation by comparing the electronic density of states (DOS) of O, N, H and the cations coordinated to the defects. By such DOS analysis, we obtain fundamental insight into the relative stability of the different nitrogen defects, as well as the position of the N-2p states relative to the valence band maximum (VBM). The latter property of nitrogen doping has gained interest particularly for applications within photocatalysis.

2 Computational details

The formation energies of point defects were calculated from the total energy difference between the defective and perfect supercells according to

$$\Delta G_{\text{defect}}^f = E_{\text{defect}}^{\text{tot}} - E_{\text{bulk}}^{\text{tot}} + \sum_i \Delta n_i \mu_i + q\mu_e \tag{8}$$

where Δn_i is the number of constituent atoms exchanged upon defect formation, q is the charge state of the defect, μ_e is the Fermi level and μ_i are the atomic chemical potentials which define the environmental conditions. Their standard states for gaseous species were taken as

$$\mu_N^\circ = \frac{1}{2}E^{\text{tot}}(N_2) \tag{9}$$

$$\mu_H^\circ = \frac{1}{2}E^{\text{tot}}(H_2) \tag{10}$$

$$\mu_{H_2O}^\circ = E^{\text{tot}}(H_2O) \tag{11}$$

The results from calculations at 0 K were extrapolated to finite temperatures by including the temperature and pressure dependency of μ_i according to

$$\mu_i(T,p) = \mu_i^\circ(T,p^\circ) + k_B T \ln(p/p^\circ) \tag{12}$$

where the temperature dependency of μ° was obtained from thermochemical tables[20] as described in ref. 21. In this respect, we assume that the entropy change of the defect reaction is dominated by the consumption and creation of gaseous species, and thus neglect the vibrational entropy contributions from the solids.[22] The oxygen chemical potential was obtained through the equilibrium between H_2O and H_2

$$\mu_O = \mu_{H_2O} - \mu_{H_2} \tag{13}$$

In this way, μ_O is controlled by varying the ratio of the H_2O and H_2 partial pressures and we thus avoid using the O_2 molecule for which the calculated binding energy includes a sizeable error within the GGA.[23,24] Finally, the concentration of defect j, c_j, was obtained through

$$c_j = \frac{N_j \exp\left(-\frac{\Delta G_{\text{defect}}^f}{k_B T}\right)}{1 + \exp\left(-\frac{\Delta G_{\text{defect}}^f}{k_B T}\right)} \tag{14}$$

where N_j is the number of defect sites per unit volume. The equilibrium Fermi level was obtained by imposing the electro-neutrality condition, $\sum_j q_j c_j = 0$.

All calculations were performed within the DFT formalism utilizing the projector augmented wave (PAW)[25] method as implemented in VASP.[26–28] Exchange and correlation was described with the generalized gradient approximation functional by Perdew, Burke and Ernzerhof (GGA-PBE).[29] Brillouine zone integration was performed according to a Γ-centered Monkhorst–Pack[30] scheme (see Table 1) and a plane wave basis set with a cut-off energy of 500 eV was employed. Spin polarized calculations were performed for defects containing odd number of electrons *i.e.* $N_O^\times$. The electrostatic interaction between charged point defects and the neutralizing background charge was corrected by aligning the core levels of the defective system to that of the perfect one.[31,32] All atomic positions, cell parameters and shapes were optimized until the residual forces for the relaxed atoms were within 0.02 eV Å^{-1} with an energy convergence of 10^{-6} eV for self-consistency. Computational parameters for all systems are summarized in Table 1.

Selected defect calculations were performed with the semi-empirical DFT-D correction due to Grimme[33] in order to

Table 1 Computational parameters: k-point grid in the supercell, supercell size and corresponding number of atoms in the supercell and the number of electrons treated as free in the cation potential. For oxygen and nitrogen, 2s and 2p electrons were treated as valence

	k-Point grid	Supercell size	Cation valence electrons
Al_2O_3	$2 \times 2 \times 2$	$3 \times 3 \times 1$ (270)	3
MgO	$2 \times 2 \times 2$	$3 \times 3 \times 3$ (216)	8
CaO	$2 \times 2 \times 2$	$3 \times 3 \times 3$ (216)	8
SrO	$2 \times 2 \times 2$	$3 \times 3 \times 3$ (216)	10
In_2O_3	$1 \times 1 \times 1$	$2 \times 2 \times 2$ (640)	13
$RE_2O_3{}^a$	$1 \times 1 \times 1$	$2 \times 2 \times 2$ (640)	11
m-ZrO_2	$2 \times 2 \times 2$	$3 \times 3 \times 3$ (324)	12
TiO_2	$2 \times 2 \times 2$	$3 \times 3 \times 4$ (216)	10
SnO_2	$2 \times 2 \times 2$	$3 \times 3 \times 4$ (216)	14
$BaZrO_3$	$2 \times 2 \times 2$	$4 \times 4 \times 4$ (320)	10/12
$SrZrO_3$	$2 \times 2 \times 2$	$3 \times 3 \times 2$ (360)	10/12

^{a} RE = Sc, Y, La.

account for dispersion effects which have been found relevant in other periodic systems.[34] While it should be noted that the correction apparently can be significant in some cases, *e.g.*, 16.5% lower formation energy of $NH_O^{\times}$ in Al_2O_3, the results were rather inconsistent with respect to the chemical nature of the considered defects as seen from their atomistic and electronic structure. The physical basis of this correction for defect calculations therefore appears uncertain at this stage and we leave this issue to be fully addressed in future studies.

3   Results and discussion

3.1   Defect energetics and electronic structure

Substitutional nitrogen, N_O^q, is found to be a deep acceptor in all the investigated oxides with the $\varepsilon(0/-1)$ transition level located 0.25–1.27 eV above the valence band maximum (Table 2). Accordingly, when N_O' is in majority they cannot be fully charge compensated by electron holes. Under the reducing and nitriding conditions considered in Section 3.2, the Fermi level is significantly higher than the $\varepsilon(0/-1)$ transition level. Thus, N_O' is considerably more stable than $N_O^{\times}$, and substitutional nitrogen will therefore predominately exist in the fully ionized charge state (N^{3-}).

Table 2 The $\varepsilon(0/-1)$ transition level for N_O^q, the upper position of N-2p states in $NH_O^{\times}$, $\varepsilon_{NH_O^{\times}}^{max}$, and the binding energies for $NH_O^{\times}$ and $(NH_2)_O^{\bullet}$, $\Delta E_{NH_O^{\times}}^b$ and $\Delta E_{(NH_2)_O^{\bullet}}^b$, respectively

	$\varepsilon(0/-1)$ (eV)	$\varepsilon_{NH_O^{\times}}^{max}$ (eV)	$\Delta E_{NH_O^{\times}}^b$ (eV)	$\Delta E_{(NH_2)_O^{\bullet}}^b$ (eV)
Al_2O_3	1.14	0.53	−2.06	−0.58
MgO	0.94	0.52	−2.10	−0.84
CaO	1.18	0.55	−1.84	−0.96
SrO	1.27	0.66	−1.99	−0.76
TiO_2	0.25	0.34	−0.35	0.01
SnO_2	1.01	0.07	−1.34	0.66
ZrO_2	0.41	0.55	−0.64	−0.56
In_2O_3	0.63	0.36	−1.30	−0.23
Sc_2O_3	0.72	0.46	−0.99	−0.06
Y_2O_3	1.17	0.44	−1.65	−0.35
La_2O_3	0.74	0.66	−1.37	−0.39
$BaZrO_3$	0.60	0.45	−1.14	−0.70
$SrZrO_3$	0.64	0.73	−1.01	−0.73

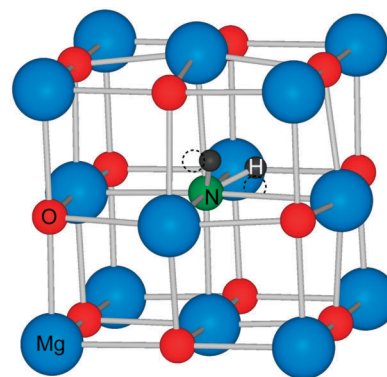**Fig. 1**   The relaxed structure of MgO containing $(NH_2)_O^{\bullet}$. For comparison, the equivalent lowest energy proton positions in $OH_O^{\bullet}$ and $NH_O^{\times}$, which lie on the connecting line to the nearest neighbour oxide ions, are marked with dashed circles.

The bond length to the proton is consistently only 2–5% longer for $NH_O^{\times}$ and $(NH_2)_O^{\bullet}$ compared to $OH_O^{\bullet}$ regardless of the binding energy. Further, the protons in $(NH_2)_O^{\bullet}$ tend to relax away from the lowest energy proton position in $OH_O^{\bullet}$ and $NH_O^{\times}$, with a resultant H–N–H angle closer to that of the NH_3 molecule (Fig. 1). The stability of $(NH_2)_O^{\bullet}$ can thus be expected to be lowered due to a steric contribution related to the geometry between the lowest energy proton positions.

The $NH_O^{\times}$ binding energy, $\Delta E_{NH_O^{\times}}^b$ (enthalpy of reaction (1)), is negative (exothermic) for all the investigated oxides, ranging from −0.35 to −2.10 eV (*cf.* Table 2). Li *et al.*[15] obtained an $NH_O^{\times}$ binding energy in the same range in ZnO from DFT calculations, −0.95 eV. With the exception of TiO_2 and SnO_2, $(NH_2)_O^{\bullet}$ also exhibits negative binding energy according to reaction (2). The binding energies can be visualized from the formation energies of the relevant defects as exemplified for CaO in Fig. 2.

The enthalpy of mobility for protons is typically in the range of 0.3–1 eV for these oxides.[35,36] By comparison with the binding energies in Table 2, it is clear that N_O' will be a strong proton trap. Although the $NH_O^{\times}$ site still remains active for proton migration since it can accommodate an additional proton by forming $(NH_2)_O^{\bullet}$, the binding energies of $(NH_2)_O^{\bullet}$ are relatively large for most of the oxides as well (*cf.* Table 2). We therefore conclude that significant amounts of nitrogen will severely reduce proton conduction in all of the investigated oxides except possibly TiO_2, Sc_2O_3 and In_2O_3.

Further evaluation of the electronic structure of $NH_O^{\times}$ and $(NH_2)_O^{\bullet}$ is necessary to gain physical insight into the nature of their binding energies. This can be obtained from the site projected density of states of N, H, O (bulk and bound to H) and the nearest neighbour cations coordinated to the defects. The binding energies can thereby be associated with the energy shift of cation, anion and proton states according to reactions (1) and (2). Fig. 3 shows the site projected DOS for $OH_O^{\bullet}$, N_O', $O_O^{\times}$, $NH_O^{\times}$ and $(NH_2)_O^{\bullet}$ in CaO. From the difference in the position of the N-states in $NH_O^{\times}$ and $(NH_2)_O^{\bullet}$ compared to N_O', it is clear that nitrogen is significantly stabilized by protons: the N-2s and N-2p states are successively shifted to lower energies in $NH_O^{\times}$ and $(NH_2)_O^{\bullet}$. The H-states, which overlap with the N-states, are also shifted to lower energy in $(NH_2)_O^{\bullet}$
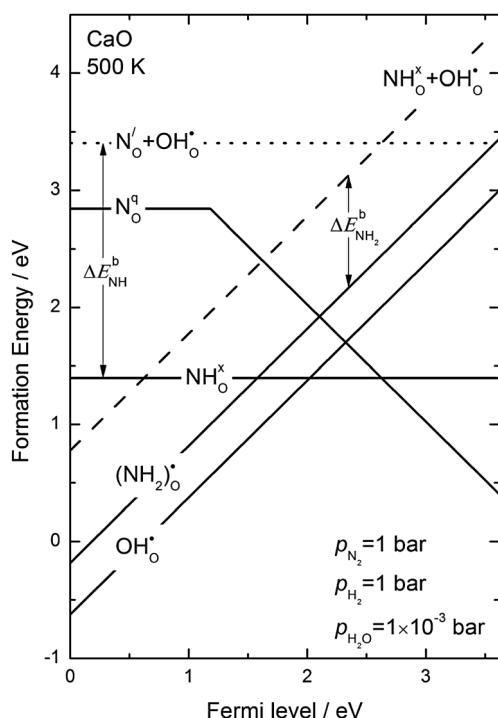
Fig. 2 Defect formation energies for CaO at 500 K and otherwise given conditions as a function of the Fermi level within the theoretical band gap, showing the binding energies of $NH_O^\times$ and $(NH_2)_O^\bullet$.
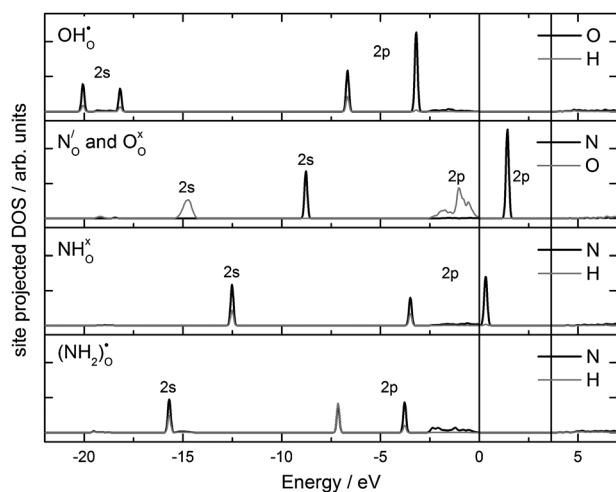

Fig. 3 Site projected DOS of the anions and protons in $OH_O^\bullet$, $O_O^\times$, N_O', $NH_O^\times$ and $(NH_2)_O^\bullet$ in CaO. The theoretical band gap is indicated with solid lines and the VBM is referenced to 0 eV.

compared to $NH_O^\times$. Still, the H-states are lowest in energy when bound to O in $OH_O^\bullet$, but, more importantly, the stabilization of the O-2s and O-2p states in $OH_O^\bullet$ compared to bulk ($O_O^\times$) is even larger than that of N-2s and N-2p states in $NH_O^\times$ and $(NH_2)_O^\bullet$ compared to N_O'. The net energy shift of the anion and proton states according to reaction (1) therefore ends up positive, *i.e.* non-binding, and thereby cannot account for the negative binding energy of $NH_O^\times$. For similar reasons, the net energy shift of the anion and proton states according to reaction (2) also ends up positive.

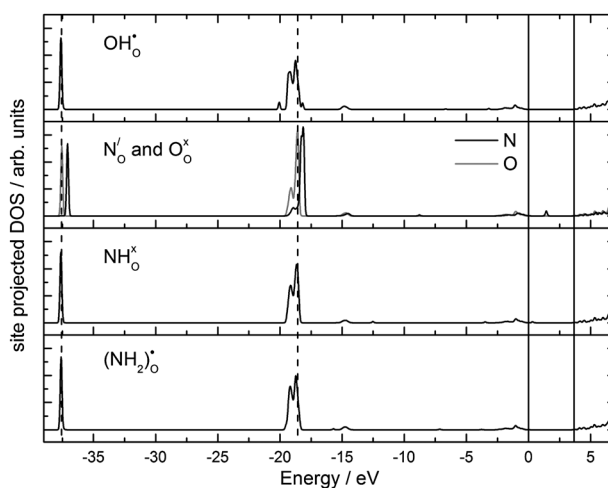**Fig. 4** Site projected DOS for the nearest neighbour Ca ions coordinated to $OH_O^\bullet$, $O_O^\times$, N_O', $NH_O^\times$ and $(NH_2)_O^\bullet$ in CaO. The position of the peak for the bulk Ca states are indicated with dashed lines. The theoretical band gap is indicated with solid lines and the valence band maximum (VBM) is referenced to 0 eV.

Fig. 4 shows the site projected DOS for the nearest neighbour cations coordinated to N_O', $NH_O^\times$, $(NH_2)_O^\bullet$, $O_O^\times$ and $OH_O^\bullet$ in CaO. Most notably, the Ca states associated with N_O' exhibit a significant shift to higher energy compared to those associated with the other species in reaction (1) ($O_O^\times$, $OH_O^\bullet$ and $NH_O^\times$). Due to the larger amount of electrons in these cation states compared to the anion states (in Fig. 3), the net energy shifts in electronic states associated with the defects in reaction (1) therefore end up negative, *i.e.*, binding. In other words, the binding energy of $NH_O^\times$ stems from the destabilization of the Ca-states associated with N_O' relative to those associated with the products in the reaction (1). The differences in the Ca states associated with the defects in reaction (2) ($OH_O^\bullet$, $NH_O^\times$ and $(NH_2)_O^\bullet$) are more subtle: those associated with the isoelectronic species ($(NH_2)_O^\bullet$ and $OH_O^\bullet$, $NH_O^\times$ and $O_O^\times$) are quite similar, but the net energy shifts according to reaction (2) also end up as binding.

All features of the electronic DOS presented for N_O', $NH_O^\times$, $(NH_2)_O^\bullet$, $O_O^\times$, $OH_O^\bullet$ and their respective coordinated cations in CaO were similar for all of the oxides. The calculated energy changes in the DOS according to reaction (2) were consistently lower than those for reaction (1) in accordance with the lower binding energy for $(NH_2)_O^\bullet$ than for $NH_O^\times$. The energy changes from these DOS calculations could, however, not be quantitatively correlated to the binding energies as calculated from total energies (eqn (1) and Fig. 2).

In light of the similarities in the electronic structure of N_O', $NH_O^\times$ and $(NH_2)_O^\bullet$ and the origin of the binding energies of $NH_O^\times$ and $(NH_2)_O^\bullet$ for all of the oxides, we conclude that the latter defects are correctly described as individual species (similar to *e.g.* hydroxide ions, $OH_O^\bullet$), rather than electrostatically interacting particles of N_O' and $H_i^\bullet$ that form defect complexes. This consideration is supported by the N–H bond lengths, and the consistency in their magnitude, which corresponds to the proton residing within the electron cloud of nitrogen.

In the case of Al_2O_3 and TiO_2, the N-2p states in N_O' consist of three distinct peaks (as opposed to one peak in Fig. 3) overlapping with the cations, indicative of more covalent bonding to N_O'. This may be related to the existence of stable and relatively covalent nitrides in these systems e.g. AlN and TiN.

An important feature in the electronic structure of N_O', $NH_O^\times$ and $(NH_2)_O^\bullet$ is the position of the N-2p states relative to the VBM. The N-2p states in N_O' are isolated above the VBM with the topmost states at the $\varepsilon(0/-1)$ level (see Table 2). However, as the N-2p states are shifted to lower energy in $NH_O^\times$ ($\varepsilon_{NH_O^\times}^{max}$ in Table 2), they approach and/or overlap with the VBM, whereas those in $(NH_2)_O^\bullet$ are located below the VBM. In other words, $NH_O^\times$ can be more effective than N_O' in raising the VBM and thereby narrowing the band gap. It should be noted that concentration effects, which are not considered in the present work, can be significant in this respect, as reported for TiO_2.[37] The $NH_O^\times$ binding energy can be loosely correlated to the lowering of the N-2p states in $NH_O^\times$ relative to N_O' i.e. $\varepsilon_{NH_O^\times}^{max} - \varepsilon(0/-1)$. As already discussed, the discrepancy in this correlation originates from the energy shift of the cation states which also contributes to $\Delta E_{NH_O^\times}^b$.

3.2 Defect structure

The similarities in the nitrogen related defect structure between all of the investigated oxides are striking: reaction (4) ($NH_O^\times$) predominates at low temperature while reaction (3) (N_O' and $V_O^{\bullet\bullet}$) predominates at high temperature in all cases. Due to these similarities, we will present the complete defect structure of undoped, acceptor- and donor doped Y_2O_3, and only tabulate the reaction enthalpies for the rest of the oxides. Fig. 5a shows the Gibbs energy of reactions (3)–(7) for Y_2O_3 in 1 bar N_2 and H_2 and 1×10^{-7} bar H_2O, i.e., a very dry and thus reducing $N_2 + H_2$ mixture. Fig. 5b shows the defect concentrations under the same conditions as calculated from the individual defect formation energies by imposing the electroneutrality condition. Fig. 5a and b reveal essentially the same behaviour for the undoped material: reaction (4) ($NH_O^\times$)

predominates up to 1450 K and reaction (3) ($[N_O'] = 2[V_O^{\bullet\bullet}]$) predominates above this temperature. The predominating charge compensating defect for N_O' is $OH_O^\bullet$ up to approximately 1000 K and $V_O^{\bullet\bullet}$ at higher temperatures. The large negative binding energy for $NH_O^\times$ (Table 2) (which means that reaction (1) is shifted to the right), is reflected by the low concentration of the isolated defects when these charge compensate each other (<950 K Fig. 5b). At the highest temperature, ΔG_3 approaches 0 and the obtained concentrations of N_O' and $V_O^{\bullet\bullet}$ approach values corresponding to a $Y_2N_2\square$ stoichiometry. In this respect, it should be noted that the concentration dependency of the defect formation energies can be considerable when approaching such high defect concentrations. The overall agreement between Fig. 4a and b means that reactions (3)–(7), and $\Delta E_{NH_O^\times}^b$ and $\Delta E_{(NH_2)_O^\bullet}^b$ appropriately describe the defect chemistry of the considered system.

Fig. 6a presents the defect concentrations when a constant concentration of a cation acceptor dopant is introduced into Y_2O_3; reaction (7) ($OH_O^\bullet$) predominates at low temperatures and $V_O^{\bullet\bullet}$ starts to take over as ΔG_7 changes sign at 650 K. In comparison with undoped Y_2O_3 (Fig. 5b), acceptor doping suppresses the predominance of nitrogen defects. In the case of donor doping (Fig. 6b), O_i'' is the predominating charge compensating defect at low temperature. In comparison, the concentration of N_i''' is minute and peaks at 6×10^{-11} mol fraction at 850 K. Donor doping clearly promotes the concentration of N_O' which predominates at as low as 815 K in the given atmosphere.

Fig. 7 shows defect concentrations in undoped Y_2O_3 as a function of temperature for a simulated quenching in which the total equilibrium nitrogen content at 1473 K from Fig. 5b is kept constant, i.e. frozen in, while oxygen and hydrogen are equilibrated with the atmosphere due to their expected higher diffusivity.[38] The defect structure is then governed by the binding energies of $NH_O^\times$ and $(NH_2)_O^\bullet$ (reactions (1) and (2)) and electroneutrality according to $2[V_O^{\bullet\bullet}] + [OH_O^\bullet] + [(NH_2)_O^\bullet] = [N_O']$. Again, the large negative binding energy of $NH_O^\times$ dominates the defect structure when the total amount of N defects is frozen. Furthermore, in
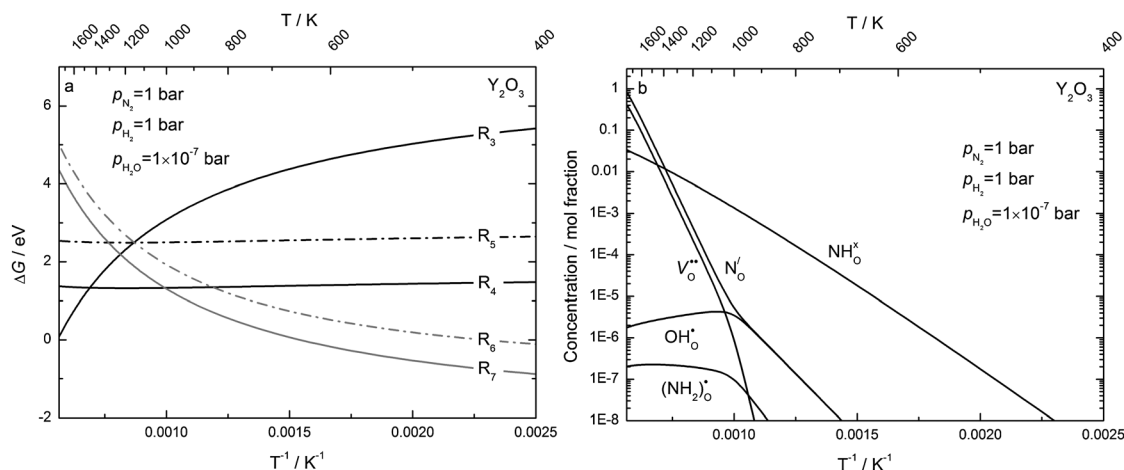

Fig. 5 Gibbs energy of reactions (3)–(7) for Y_2O_3 (a) and corresponding defect concentrations (b) in 1 bar N_2 and H_2 and 1×10^{-7} bar H_2O. Reactions (6) and (7) (grey) involve consumption of oxygen vacancies and can therefore predominate only if the material is acceptor doped.
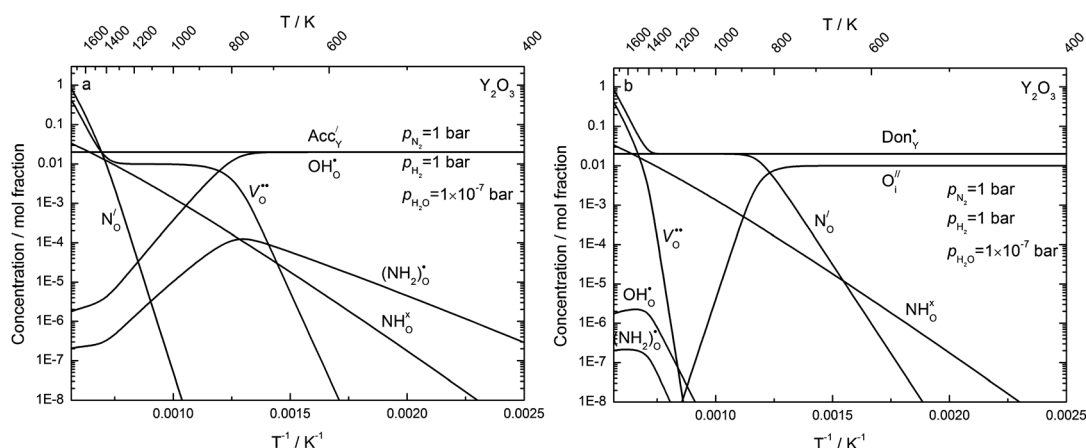
Fig. 6 Defect concentrations as a function of temperature in 1 cation mol% acceptor doped (a) and donor doped (b) Y_2O_3.
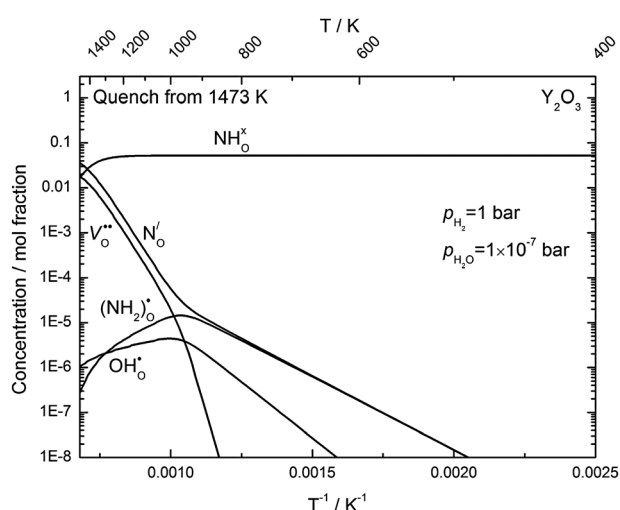

Fig. 7 Defect concentrations as a function of temperature when the equilibrium nitrogen content at 1473 K in Fig. 4b is kept constant (frozen in).

contrast to the equilibrium case (Fig. 5b), the negative binding energy of $(NH_2)_O^\bullet$ becomes apparent as this defect becomes the predominating effectively positive defect below approximately 1000 K.

The calculated defect structure of Y_2O_3 is in good agreement with our experimental work on Y_2O_3 where we proposed that $NH_O^\times$ was the predominating nitrogen defect based on electrical conductivity measurements at 1273–1473 K in an NH_3 atmosphere.[17] Furthermore, the concentration of $NH_O^\times$ in specimens quenched at 1473 K in NH_3 was estimated to be 7×10^{-3} mol fraction.[17] Considering the uncertainties in p_{O_2}, p_{H_2O} and p_{NH_3} in the experimental setup and the amount of nitrogen that diffuses out during quenching (not considered in Fig. 7), the calculated $NH_O^\times$ concentration, 5×10^{-2} mol fraction, can be asserted to be in good agreement with the experimental value.

The calculated enthalpies of reactions (3)–(7) for all of the investigated oxides are summarized in Table 3. The enthalpy of reaction (4) is the lowest for all compounds except for ZrO_2, where the enthalpy of reaction (5) is slightly lower. Still, as shown in Fig. 8, the concentrations of $NH_O^\times$ and N_O' are essentially identical at low temperatures. It should be noted that, while the amount of nitrogen incorporated per unit reaction through reactions (3)–(6) is identical, the total number of defects formed differ. Thus, the reaction (or combination of reactions) with the lowest Gibbs energy does not necessarily correspond to the predominating defect situation. The calculated hydration enthalpies, ΔH_7, are in good agreement with experimental values with a maximum deviation of 20% for TiO_2.

Table 3 Calculated enthalpies for reactions (3)–(7) at 0 K. The defects which are created and consumed in reactions are shown. All values are in eV. The negative enthalpy of reaction (4) for SnO_2 reflects the instability of the material with respect to NH_3

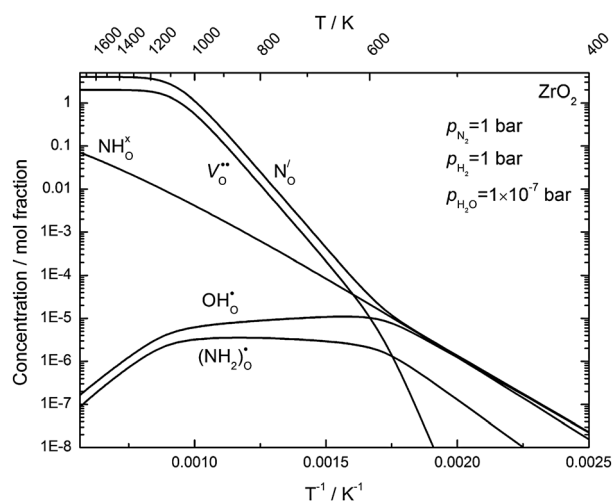| | ΔH_3 | ΔH_4 | ΔH_5 | ΔH_6 | ΔH_7 | ΔH_7^{exp} |
	$2N_O' + V_O^{\bullet\bullet}$	$2NH_O^\times$	$(NH_2)_O^\bullet + N_O'$	$2(NH_2)_O^\bullet - V_O^{\bullet\bullet}$	$2OH_O^\bullet - V_O^{\bullet\bullet}$	
Al_2O_3	7.44	2.62	3.87	0.31	−1.17	
MgO	8.00	3.92	4.88	1.76	−0.47	
CaO	8.16	3.12	3.96	−0.23	−1.43	
SrO	7.99	2.74	3.83	−0.34	−1.56	
TiO_2	2.87	0.69	0.95	−0.98	−1.69	−1.35[36]
SnO_2	3.69	−0.94	0.84	−2.01	−2.39	
ZrO_2	4.09	1.81	1.77	−0.55	−1.23	
Sc_2O_3	6.06	2.03	3.00	−0.06	−1.63	
In_2O_3	3.91	1.02	1.82	−0.26	−1.16	
Y_2O_3	7.13	1.95	3.13	−0.88	−2.12	−2.09[39]
La_2O_3	6.39	1.80	2.74	−0.90	−1.92	
$BaZrO_3$	5.55	2.59	4.25	0.48	−0.71	−0.84[40]
$SrZrO_3$	5.45	2.31	2.58	−0.29	−1.14	−1.10[41]

Fig. 8 Defect concentrations in ZrO_2 under 1 bar N_2 and 1 bar H_2 and 1×10^{-7} bar H_2O.
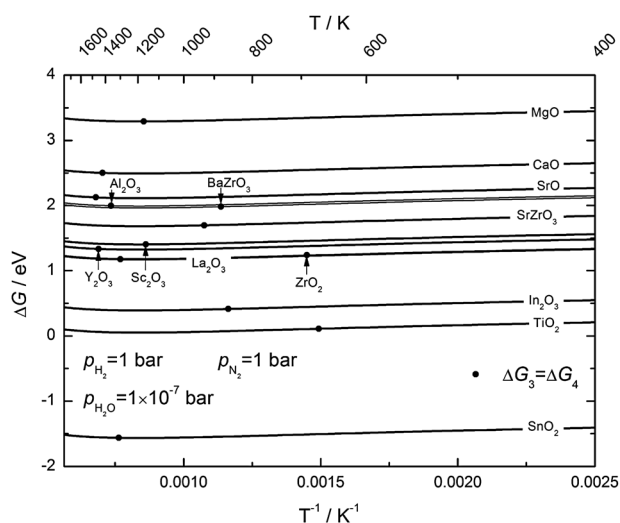

Fig. 9 Gibbs energy of reaction (4) in 1 bar N_2 and H_2 and 1×10^{-7} bar H_2O. The bullet on each graph represents the temperature at which reaction (3) becomes predominating. The negative Gibbs energies for SnO_2 reflect the instability of the material which will be reduced under these conditions.

Fig. 9 shows the Gibbs energy of reaction (4) ($NH_O^\times$) as well as the temperature at which reaction (3) ($2N_O' + V_O^{\bullet\bullet}$) becomes predominating for all of the investigated oxides. Amongst the oxides with the lowest transition temperature are TiO_2, ZrO_2 and the perovskites which are all materials where considerable amounts of $V_O^{\bullet\bullet}$ can be introduced by acceptor doping. Furthermore, the oxides, which exhibit the lowest enthalpies of reactions (2) and (3) (SnO_2, TiO_2, In_2O_3 and ZrO_2), also exhibit the lowest formation enthalpies (per mole O_2). It should be noted that the transition temperature is independent of the atmospheric conditions since the relative chemical potential dependencies of reactions (3) and (4) remain unchanged. In most compounds the concentration of $NH_O^\times$ will be predominating or significant under typical conditions for equilibrium nitrogen incorporation e.g. 900–1300 K in an NH_3 atmosphere. Thus, nitrogen incorporation will be facilitated

by the presence of hydrogen, especially under conditions where reaction (4) is most favourable, as demonstrated for ZnO.[42]

Finally, it is reasonable to assume that the corrosion resistance of oxides in nitriding atmospheres will depend on their defect structure and thereby exhibit a transition between the two predominating defect situations, i.e., $NH_O^\times$ and $2N_O' + V_O^{\bullet\bullet}$. In this respect, one may speculate whether reaction (3) ($2N_O' + V_O^{\bullet\bullet}$) is more deteriorating for the oxide compared to reaction (2) ($NH_O^\times$) since it involves a larger number of defects and it includes formation of oxygen vacancies which enables faster anion diffusion. By this argumentation, MgO, CaO, SrO and Al_2O_3, all exhibiting high reaction energies and high transition temperatures (Fig. 9), will exhibit the highest corrosion resistance towards nitriding atmospheres, and the otherwise excellent refractory oxide ZrO_2 can be expected to be inferior in comparison.

4 Summary and conclusion

The nitrogen related defect chemistry of oxides has been evaluated based on first principles DFT calculations of $N_O^\times$, N_O', $NH_O^\times$, $(NH_2)_O^\bullet$, $V_O^{\bullet\bullet}$ and $OH_O^\bullet$ defects in rocksalt MgO, CaO and SrO; corundum Al_2O_3; C-type In_2O_3, Sc_2O_3, Y_2O_3 and La_2O_3; rutile TiO_2 and SnO_2; monoclinic ZrO_2; and perovskite $BaZrO_3$ and $SrZrO_3$. The defect structure as well as the atomistic and electronic structure of nitrogen were found to be similar within all of the oxides. Specifically, $NH_O^\times$ predominates at low temperatures while N_O' and $V_O^{\bullet\bullet}$ predominate at high temperature. The transition temperature between these two defect situations was found to be above 900 K for most of the oxides and at approximately 650 K for TiO_2 and ZrO_2. This means that $NH_O^\times$ can be the predominating nitrogen defect when oxide specimens are equilibrated in nitriding atmospheres under typical experimental conditions, e.g. 600–1200 K in NH_3. Hence, the solubility of substitutional nitrogen in these oxides is facilitated by the presence of hydrogen. Nitrogen interstitials, N_i''', were considered in some of the compounds in which O_i'' are important (e.g. Y_2O_3), but their concentration was found to be negligible even in donor doped material under reducing conditions. N_O^q was found to be a deep acceptor in all the investigated oxides which means that they cannot be thermally ionized (by excitation of electrons from VBM) and fully charge compensated by electron holes.

The binding energy of $NH_O^\times$ was found to be negative, i.e. binding, in all of the investigated oxides. This is consistent with the predominance of $NH_O^\times$ over its dissociated counterparts, N_O' and $OH_O^\bullet$, when these defects coexist. In combination with the relatively negative binding energy for $(NH_2)_O^\bullet$ in most of the investigated oxides, we conclude that nitrogen incorporation can be expected to severely inhibit the proton conductivity of oxides. Through semi-quantitative analysis of the electronic DOS, the nature of the binding energy of $NH_O^\times$ could be linked to the relative instability of cations coordinated to N_O'. Finally, while the N-2p states in N_O' are isolated above the VBM, they are shifted towards or overlap with the VBM in $NH_O^\times$. Thus, in terms of band gap engineering, $NH_O^\times$ may be more suitable than N_O' for shifting the VBM to higher energy and thus lower the band gap of oxides.

Acknowledgements

References

1 Ü. Özgür, Y. I. Alivov, C. Liu, A. Teke, M. A. Reshchikov, S. Doğan, V. Avrutin, S. J. Cho and H. Morkoç, *J. Appl. Phys.*, 2005, **98**, 041301.

2 J. L. Lyons, A. Janotti and C. G. Van de Walle, *Appl. Phys. Lett.*, 2009, **95**, 252105.

3 V. Avrutin, D. J. Silversmith and H. Morkoç, *Proc. IEEE*, 2010, **98**, 1269–1280.

4 A. B. Jorge, J. Fraxedas, A. Cantarero, A. J. Williams, J. Rodgers, J. P. Attfield and A. Fuertes, *Chem. Mater.*, 2008, **20**, 1682–1684.

5 M. Lerch, *J. Am. Ceram. Soc.*, 1996, **79**, 2641–2644.

6 F. Tessier and R. Marchand, *J. Solid State Chem.*, 2003, **171**, 143–151.

7 M. Lerch, *J. Mater. Sci. Lett.*, 1998, **17**, 441–443.

8 N. Diot, O. Larcher, R. Marchand, J. Y. Kempf and P. Macaudière, *J. Alloys Compd.*, 2001, **323**, 45–48.

9 P. Maillard, F. Tessier, E. Orhan, F. Cheviré and R. Marchand, *Chem. Mater.*, 2005, **17**, 152–156.

10 Y. B. Cheng and D. P. Thompson, *J. Am. Ceram. Soc.*, 1993, **76**, 683–688.

11 J. Wendel, M. Lerch and W. Laqua, *J. Solid State Chem.*, 1999, **142**, 163–167.

12 J. S. Lee, J. Fleig, J. Maier, D. Y. Kim and T. J. Chung, *J. Am. Ceram. Soc.*, 2005, **88**, 3067–3074.

13 T. Bredow, *Phys. Rev. B: Condens. Matter Mater. Phys.*, 2007, **75**, 144102.

14 S. J. Jokela and M. D. McCluskey, *Phys. Rev. B: Condens. Matter Mater. Phys.*, 2007, **76**, 193201.

15 X. N. Li, B. Keyes, S. Asher, S. B. Zhang, S. H. Wei, T. J. Coutts, S. Limpijumnong and C. G. Van de Walle, *Appl. Phys. Lett.*, 2005, **86**, 122107.

16 T. S. Bjørheim, S. Stølen and T. Norby, *Phys. Chem. Chem. Phys.*, 2010, **12**, 6817–6825.

17 J. M. Polfus, R. Haugsrud and T. Norby, *Dalton Trans.*, 2011, **40**, 132–135.

18 J. M. Polfus, K. Toyoura, C. Hervoches, M. Sunding, I. Tanaka and R. Haugsrud, *J. Mater. Chem.*, DOI: 10.1039/c2jm16202d.

19 H. Boysen, I. Kaiser-Bischoff, M. Lerch, S. Berendts, M. Hoelzel and A. Senyshyn, *Acta Phys. Pol., A*, 2010, **117**, 38–41.

20 M. Chase Jr, *J. Phys. Chem. Ref. Data, Monogr.*, 1998, **9**.

21 A. Kuwabara, *Sci. Technol. Adv. Mater.*, 2007, **8**, 519–523.

22 M. E. Björketun, P. G. Sundell and G. Wahnström, *Faraday Discuss.*, 2007, **134**, 247–265.

23 I. G. Batyrev, A. Alavi and M. W. Finnis, *Phys. Rev. B: Condens. Matter Mater. Phys.*, 2000, **62**, 4698–4706.

24 B. Meyer, *Phys. Rev. B: Condens. Matter Mater. Phys.*, 2004, **69**, 045416.

25 P. E. Blöchl, *Phys. Rev. B: Condens. Matter Mater. Phys.*, 1994, **50**, 17953–17979.

26 G. Kresse and J. Hafner, *Phys. Rev. B: Condens. Matter Mater. Phys.*, 1993, **48**, 13115–13118.

27 G. Kresse and J. Furthmüller, *Phys. Rev. B: Condens. Matter Mater. Phys.*, 1996, **54**, 11169–11186.

28 G. Kresse and D. Joubert, *Phys. Rev. B: Condens. Matter Mater. Phys.*, 1999, **59**, 1758–1775.

29 J. P. Perdew, K. Burke and M. Ernzerhof, *Phys. Rev. Lett.*, 1996, **77**, 3865–3868.

30 H. J. Monkhorst and J. D. Pack, *Phys. Rev. B: Solid State*, 1976, **13**, 5188–5192.

31 C. G. Van de Walle and J. Neugebauer, *J. Appl. Phys.*, 2004, **95**, 3851–3879.

32 F. Oba, M. Choi, A. Togo and I. Tanaka, *Sci. Technol. Adv. Mater.*, 2011, **12**, 034302.

33 S. Grimme, *J. Comput. Chem.*, 2006, **27**, 1787–1799.

34 D. K. Ward, X. W. Zhou, B. M. Wong, F. P. Doty and J. A. Zimmerman, *Phys. Rev. B: Condens. Matter Mater. Phys.*, 2012, **85**, 115206.

35 T. Norby and Y. Larring, *Curr. Opin. Solid State Mater. Sci.*, 1997, **2**, 593–599.

36 S. Erdal, C. Kongshaug, T. S. Bjørheim, N. Jalarvo, R. Haugsrud and T. Norby, *J. Phys. Chem. C*, 2010, **114**, 9139–9145.

37 K. S. Yang, Y. Dai and B. B. Huang, *J. Phys. Chem. C*, 2007, **111**, 12086–12090.

38 M. Lerch, J. Janek, K. D. Becker, S. Berendts, H. Boysen, T. Bredow, R. Dronskowski, S. G. Ebbinghaus, M. Kilo, M. W. Lumey, M. Martin, C. Reimann, E. Schweda, I. Valov and H. D. Wiemhöfer, *Prog. Solid State Chem.*, 2009, **37**, 81–131.

39 Y. Larring and T. Norby, *Solid State Ionics*, 1997, **97**, 523–528.

40 C. Kjølseth, L. Y. Wang, R. Haugsrud and T. Norby, *Solid State Ionics*, 2010, **181**, 1740–1745.

41 F. Krug and T. Schober, *J. Am. Ceram. Soc.*, 1997, **80**, 794–796.

42 T. Yamamoto, *Thin Solid Films*, 2002, **420**, 100–106.

This journal is © the Owner Societies 2012

Phys. Chem. Chem. Phys., 2012, **14**, 11808–11815 | 11815